Design, Modeling and Control of an Optical Pointing Sensor for the Formation Control Testbed (FCT)

Joel Shields*, Brandon Metz , Randy Bartos , Arin Morfopoulos , Chuck Bergh, Jason Keim , Dan Scharf and Asif Ahmed

Jet Propulsion Laboratory, California Institute of Technology, Pasadena, CA, 91109, USA

In this paper the design and modeling of a sensor system that gives relative position measurements is described. The position is provided in the form of bearing and range to a retro target placed on a far field target.

The system uses two laser sources. An off the shelf IR laser rangefinder is used to give range measurements based on time of flight. A second 633nm source is used in conjunction with a fast steering mirror (FSM) and shear sensor on the backend of the optical path to control and detect, respectively, the shear at the retro target.

Models of the FSM, optical path and shear sensor are developed. These models are used in an end to end simulation of the system. This simulation is used for compensator design and code development. Both simulated and benchtop experimental data are presented that demonstrate an open loop spiral search of the retro target, detection and lock up of the pointing system and tracking of a moving retro target.

I. Introduction

FORMATION flying is a JPL strategic technology area. The Formation Control Testbed (FCT) is a two robot facility used for demonstrating formation control, estimation, and hardware technologies. Each robot uses spherical and linear air bearings to mimic the frictionless dynamic environment of space. Float gas for 30 minutes of operation is carried with each robot as well as battery power and a full suite of avionics. Communication between robots and to a ground station is achieved with wireless modems. For actuation, each robot has cold gas thrusters and reactions wheels. For sensing, a camera system on each robot is used to determine attitude and position (pose) relative to a room frame. Fiber optic gyros are used to smooth the attitude estimates. For determination of relative position, the robots currently communicate and then difference each others pose data. The next step in formation complexity is to add direct relative sensing using the optical pointing sensor described in this paper.

The optical pointing sensor is a steerable IR rangefinder that gives range and bearing measurements to a passive retro-reflector target. The retro is placed on one robot and the rangefinder and steering optics on the other robot. The measurements are available on the rangefinder mounted robot giving it relative position knowledge to the retro.

The system is composed of a HeNe pointing laser at 633 nm, an SICK IR laser rangefinder operating at 905 nm, a two axis fast steering mirror, a shear sensor, and the far field retro. The pointing laser is injected into the optical path using a beam splitter and bounces off the steering mirror toward the retro. If the retro is hit by the pointing laser, the beam is returned with the exact opposite direction. When the beam impact with the retro is noncentral, the return will be separated (sheared) from the outgoing beam by twice the distance between the impact point and the center of the retro. Provided the shear amount is small enough, the return will hit the aperture of the steering mirror, go back through the beam splitter and be imaged on the back end of the scanner with the shear sensor. A telescope placed in front of the shear sensor serves to compress the image of the return beam to the size of the detector.

*Senior Engineer, Jet Propulsion Laboratory, California Institute of Technology, 4800 Oak Grove Blvd., Pasadena, CA 91109. MS 198-326, email: Joel.F.Shields@jpl.nasa.gov

To acquire the retro within the field of view of the shear sensor, the system operates by first performing an open loop search for the retro target. Once a return from the retro optic is detected, a servo loop is closed with the fast steering mirror and shear sensor to center the laser beam on the vertex of the retro.

Once locked, any motion of the retro will be tracked by keeping the servo error small. Once in track mode, the IR rangefinder can be used to give range measurements. Bearing measurements are available from a local sensor used by the steering mirror.

Further details of each component of the pointing system are given in the following sections of this paper. The next section of this paper covers modeling of the fast steering mirror, optical path, and shear sensor. This is followed by a sections describing the design of the tracking filter for the shear servo and the trigger filter used by the software to determine if a return from the retro has occurred. The search trajectory used to acquire the retro is then described, followed by sections giving simulation and experimental results of the sensor system. Concluding remarks are given in the final section of this paper.

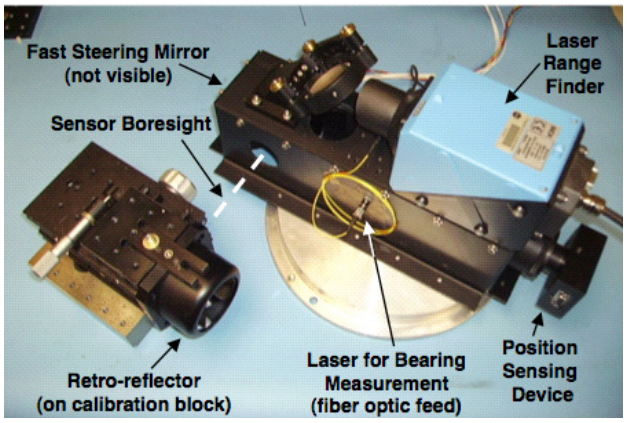

Figure 1. FCT optical pointing loop hardware. The sensor system is composed of a laser rangefinder, fast steering mirror, backend shear sensor, and a large aperture, open face, retro target.

II. Modeling

II.A. Fast Steering Mirror

The fast steering mirror used in the optical pointing system is a prototype unit developed by Left Hand Design. It uses differential inductive sensors from Kaman Measuring Systems to sense the tip and tilt of a flexured mirror. The flexure system allows for two degree of freedom rotational motion about two orthogonal axes. These axes are at the center of mass of the mirror, offset from the mirror surface by ∼5.0 mm, and allow for ±3.0 degrees of mechanical motion about either axis. The resonant frequency of the flexure is approximately 10 Hz in these two degrees of freedom and is designed to be stiff in the remaining directions. An analog compensator uses the sensor signals as feedback to electronically stiffen the flexure. Voltage inputs for servo commands and feedforward signals are integrated into the circuitry of this compensator. To actuate the mirror a voice coil motor is used. The coil is placed on the fixed base of the mechanism and pushes\pulls against magnets placed on the moving mass. In addition to moving the mirror mass, the voice coil also pushes with equal force on a dummy mass. This design feature is intended to cancel any reactions that would otherwise be transmitted to the base of the mechanism.

To model the dynamic response of this mechanism a frequency response of the analog servo was performed. This test used a chirp signal as the command to the elevation axis while holding the azimuth axis fixed. Both elevation and azimuth output voltages were monitored during the stimulus to detect cross axis coupling at high frequencies. The frequency was swept from DC to 2000 Hz at an amplitude small enough (±0.04 volts) to just avoid saturation of signals internal to the servo. Input and output data was sampled at 12.8 kHz. The data was processed off line using the empirical transfer function estimate with a frequency grid of 5 Hz.[1] The test results for the elevation axis are shown in Figure 2. The closed loop bandwidth of the mechanism is 700 Hz, but with a large amount of the axial coupling. This coupling effectively reduces the bandwidth to 200 Hz, which for our purposes is sufficient. The analog model for the elevation axis is given by,

$$\begin{aligned} G^o_{EL}(s) &= \exp\left(-0.00035\, s\right)\frac{0.001801s+1}{0.000625s+1} \\ &\quad \frac{1414}{s+1414}\,\frac{6912}{s+6912}\,\frac{s^2+1037s+2.986e6}{s^2+898.5s+2.986e6} \\ &\quad \frac{s^2+1062s+1.668e7}{s^2+980.2s+1.668e7}. \end{aligned} \tag{1}$$

This model is shown overlayed on the frequency domain data in Figure 2. A similar model was fit for the

azimuth axis. These transfer functions were used in the simulations of the optical pointing system.

The mirror of the FSM is elliptical (40 mm x 60 mm) and designed for a 45 degree incidence between an incident beam and the elevation axis and a 90 degree incidence with the azimuth axis. The mirror is situated in the optical path so that the pointing and rangefinder beams strike the mirror with these incidences. Linear and nonlinear models of the reflection kinematics at the FSM are given below.

II.B. Optical Path

The optical paths of both the IR rangefinder laser and pointing laser are depicted in Figure 3. The IR laser is injected from an overhead position to a dichroic beam splitter (Edmund Optics NT43-957). This beam splitter is designed to reflect IR wavelengths and transmit light in the visible spectrum. The reflected component of the IR is sent to the FSM mirror. A small portion (< 1.0 percent) of the IR light is transmitted at the dichroic beam splitter. To attenuate this transmitted light, a beam dump directly below the dichroic beam splitter is used to capture this light and prevent a local reflection from getting back to the rangefinder optics. Upon return from the FSM and retroreflector the IR beam again impacts the dichroic beamsplitter and is directed back up to the rangefinder optics. On the return, the small portion of IR light that is transmitted by the dichroic beam splitter is attenuated by a narrowband filter (632.8 nm, 10 nm ± 2 nm Full Width Half Maximum (FWHM), 50 percent transmittance at 632.8 nm) placed in front of the shear sensor.

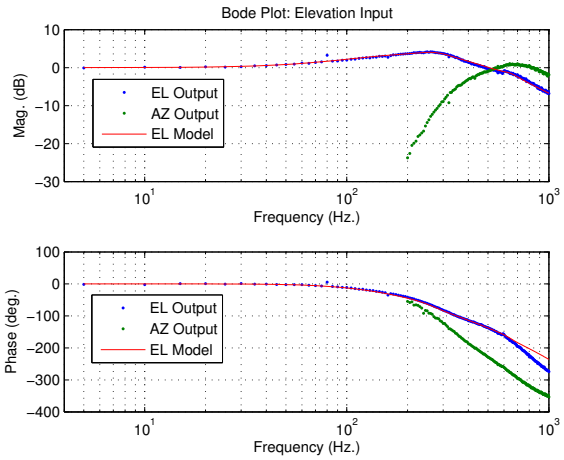

Figure 2. Frequency response of prototype Left Hand Design fast steering mirror. Response of elevation axis to chirp voltage command is shown. Azimuth axis command voltage was held at zero.

As shown in Figure 3 the pointing laser is injected at a point behind the IR laser. This beam hits a 50/50 beamsplitter (Edmund Optics NT45-854) and is reflected toward the dichroic beamsplitter. The pointing laser is transmitted by the dichroic beam splitter and sent out to the FSM and retroreflector. Assuming that the beam hits the retro, it will return with the exact opposite direction as the outgoing beam. The return beam will be sheared or offset from the outgoing beam by twice the amount of shear at the retro. The return of the pointing laser passes back through the two beamsplitters and is imaged onto a shear sensor using a refractive compressor with a compression ratio of 4. This compression ratio maps the 40 mm diameter aperture of the FSM to the 10 mm size of the detector. The shear sensor measures the shear in two orthogonal directions. The pointing servo acts to null this shear thereby keeping the pointing beam on the vertex of the retroreflector. By design the pointing laser and IR laser share the same boresight. This means the IR beam is also returned with zero shear once the shear servo is closed. This is important as the rangefinder will not operate reliably with a large amount of shear in the return. This brings up a bit of contradiction since, as we will see below, stability of the pointing loop requires knowledge of the range between the FSM and retro, but this range is not available from the rangefinder until after the pointing loop has been locked up. What is required is a rough knowledge of the range be supplied to the pointing loop prior to lockup. In the formation flying scenario this is to be accomplished with a coarse formation sensor prior to operation of the optical pointing sensor discussed in this paper.

Next we take a look at the reflections at the FSM and retroreflector in a bit more detail. Models of these reflections are developed and used in both the design and simulation of the pointing system.

II.B.1. FSM Reflection

The flexure system of the Left Hand Design FSM functions as a gimbaled azimuth/elevation mount. The azimuth axis of rotation, shown in Figure 3, is fixed to the body frame of the device whereas the elevation axis is rotated with azimuth motion. Let us define the y-axis of the FSM body frame, $\hat{\mathbf{y}}$, parallel to the azimuth axis of rotation, the x-axis, $\hat{\mathbf{x}}$, coincident with the elevation axis of rotation when the azimuth rotation is zero, and the z-axis, $\hat{\mathbf{z}}$, as the cross product of the x-axis with the y-axis. When θ_{AZ} and θ_{EL} are

both zero let the mirror normal, $\hat{\mathbf{n}}_{mirror} = \hat{\mathbf{z}}$. With these definitions, an incident beam in the frame of the FSM, $\hat{\mathbf{i}}^{MF}$, has a reflection given by,

$$\hat{\mathbf{r}}^{MF} = (\mathbf{I} - 2\,\hat{\mathbf{n}}^{MF}_{mirror}(\hat{\mathbf{n}}^{MF}_{mirror})^T)\,\hat{\mathbf{i}}^{MF}, \tag{2}$$

where $\hat{\mathbf{n}}^{MF}_{mirror}$ is determined by the azimuth and elevation rotations in the following manner.

$$\hat{\mathbf{n}}^{MF}_{mirror} = e^{\hat{\mathbf{x}}_p^{\times}\theta_{EL}} e^{\hat{\mathbf{y}}^{\times}\theta_{AZ}} \hat{\mathbf{z}}, \tag{3}$$

where the $(\cdot)^{\times}$ operator is used to denote the cross product matrix of a vector $\mathbf{v}$,

$$\mathbf{v}^{\times} = \begin{bmatrix} 0 & -v_z & v_y \\ v_z & 0 & -v_x \\ -v_y & v_x & 0 \end{bmatrix}. \tag{4}$$

In Equation (3) we have used the matrix exponential to represent the two rotations about the azimuth and elevation axes.[2] We have assumed that the azimuth rotation is done first followed by the elevation rotation, but this is of no consequence since these operations commute.[3] In Equation (3) $\mathbf{x}_p$ is the rotated elevation axis given by,

$$\hat{\mathbf{x}}^{MF}_p = e^{\hat{\mathbf{y}}^{\times}\theta_{AZ}} \hat{\mathbf{x}}. \tag{5}$$

Equations (2)-(5) are used in a simulation of the pointing system to determine the direction of the reflected beam given the incident ray direction and rotation angles θ_{AZ} and θ_{EL}. For the purposes of control system design and trajectory generation we are also interested in the linearized sensitivity of these equations about the point where θ_{AZ} and θ_{EL} are zero.

For small angles, these sensitivities can be derived by looking at the norm of the derivatives of Equation (2) with respect to θ_{AZ} and θ_{EL}. For the incidence of $\hat{\mathbf{i}}^{MF}$ described in section II.A and shown in Figure 3 these derivatives evaluate to,

$$\left\| \frac{\partial \hat{\mathbf{r}}^{MF}(\theta_{AZ},\theta_{EL})}{\partial \theta_{AZ}}\Big|_{\mathbf{0}} \right\|_2 = 2.0 \tag{6}$$

$$\left\| \frac{\partial \hat{\mathbf{r}}^{MF}(\theta_{AZ},\theta_{EL})}{\partial \theta_{EL}}\Big|_{\mathbf{0}} \right\|_2 = \frac{2.0}{\sqrt{2}}. \tag{7}$$

Equation (6) gives the change in angle of the reflected beam in the x-z plane. Equation (7) gives the change in angle of the reflected beam in the plane formed by the y-axis and the direction of the nominal reflected beam. Because of the non-normal incidence with the elevation axis, the sensitivity of the reflected beam in this direction is reduced relative to the azimuth sensitivity. This difference in sensitivity changes the loop gain of the shear sensor loop and must be taken into account when designing the compensators for this loop. A consequence of this gain difference is that the azimuth axis will have a greater error due to process (actuator) noise.

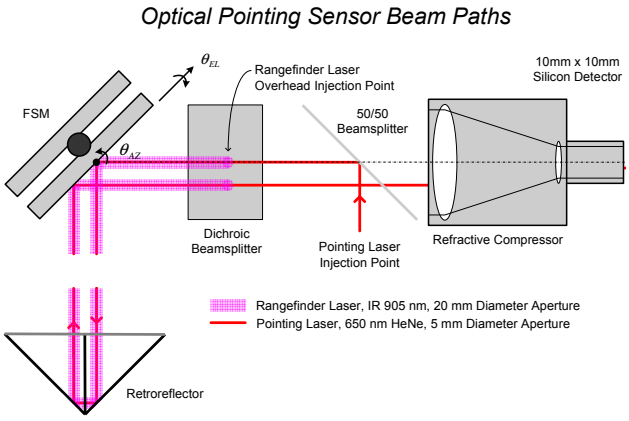

Figure 3. Diagram of beam paths for the optical pointing sensor. The diagram depicts a case with the retro offset to the left of center. This introduces shear that is sensed at the backend.

II.B.2. Corner Cube Reflections

The retro we are using is a Melles Griot 02-CCH-013 open face corner cube with an aperture of 63.5 mm, beam divergence of 1.0 arc second, and acceptance angle of 35.0 degrees. The open face eliminates the first reflection associated with solid glass retro reflectors.

A corner cube is an arrangement of three flat mirrors such that the normal of each mirror is perpendicular to the other two. It possesses the property that any ray entering the effective aperture of the retro reflector will be reflected and emerge parallel to itself, but in the opposite direction of propagation. The vertex of the corner cube, or center, is the point at which the three mirror surfaces intersect. We can define a coordinate

system for the retro by denoting this point as the origin and by using the three mirror surface lines of intersection as the x, y, and z axes of the frame. The x-axis, for example, could be the line of intersection between any two of the three mirrors. Once this axis is chosen, the other two axes are determined so that the coordinate frame is right handed. In this way the mirror in the y-z plane will have the x-axis as its normal, the mirror in the x-z plane will have the y-axis as its normal, and the mirror in the x-y plane will have the z-axis as its normal. The boresight, or centerline, of the retro is the line from the origin in the direction, $\hat{\mathbf{n}}_{bs}^{RF} = [1,1,1]/\parallel [1,1,1] \parallel_2$, where RF is used to denote the retro frame.

In order for there to be a return from the retro the incident beam must,

- Hit within a certain radius of the vertex, i.e. within what is commonly referred to as the clear aperture.
- The angle between the incident ray and retro boresight must be less than the acceptance angle of the retro.

We can model this behavior by defining a plane in front of the vertex with normal vector, $\hat{\mathbf{n}}_{bs}^{RF}$, that passes through the point, $\mathbf{v}_{front}^{RF} = \hat{\mathbf{n}}_{bs}^{RF} \cdot L_1$, where L_1 is the distance from the vertex to the front face of the retro. If we denote $\mathbf{v}_s^{RF}$ and $\hat{\mathbf{i}}_s^{RF}$ as the position and direction of the incident beam in the frame of the retro, the impact point of the incident beam on the plane of the clear aperture can be calculated as,

$$\mathbf{v}_{caip}^{RF} = \mathbf{v}_s^{RF} + \lambda^* \cdot \hat{\mathbf{i}}_s^{RF} \tag{8}$$

where,

$$\lambda^* = \frac{(\hat{\mathbf{n}}_{bs}^{RF})^T(\mathbf{v}_{front}^{RF} - \mathbf{v}_s^{RF})}{(\hat{\mathbf{n}}_{bs}^{RF})^T\,\hat{\mathbf{i}}_s^{RF}}. \tag{9}$$

The distance from the center of the clear aperture to this impact point is then,

$$R_{caip} = \parallel \mathbf{v}_{caip}^{RF} - \mathbf{v}_{front}^{RF} \parallel_2, \tag{10}$$

where R_{caip} has to be less than half the clear aperture of the retro to satisfy the the first condition for a return signal. The second condition can be checked by seeing if,

$$\begin{aligned} \theta_{FOV} \quad = \quad & \arctan 2(\parallel -\hat{\mathbf{i}}_s^{RF} - ((-\hat{\mathbf{i}}_s^{RF})^T\hat{\mathbf{n}}_{bs}^{RF})\hat{\mathbf{n}}_{bs}^{RF} \parallel_2, \\ & (-\hat{\mathbf{i}}_s^{RF})^T\hat{\mathbf{n}}_{bs}^{RF}) \end{aligned} \tag{11}$$

is less than the acceptance angle. If both of these conditions are satisfied, the point of first reflection is determined by finding the minimum of the three path lengths from the source to each of the mirror surfaces. The first reflection point is then given by,

$$\mathbf{v}_{r1}^{RF} = \mathbf{v}_s^{RF} + \lambda_{min1}^* \cdot \hat{\mathbf{i}}_s^{RF}, \tag{12}$$

where λ_{min1}^* is the minimum of the three path lengths to each of the mirrors. The direction of the first reflection is given by,

$$\hat{\mathbf{r}}_1^{RF} = (\mathbf{I} - 2\,\hat{\mathbf{n}}_{r1}^{RF}(\hat{\mathbf{n}}_{r1}^{RF})^T)\,\hat{\mathbf{i}}_s^{RF}, \tag{13}$$

where $\hat{\mathbf{n}}_{r1}^{RF}$ is the normal of the first mirror that is hit. Next we find which of the remaining two surfaces is hit next by calculating the path lengths to each of the remaining surfaces and again selecting the surface with the minimum path length. The position and direction of the secondary reflection is given by,

$$\mathbf{v}_{r2}^{RF} = \mathbf{v}_{r1}^{RF} + \lambda_{min2}^* \cdot \hat{\mathbf{r}}_1^{RF}, \tag{14}$$

$$\hat{\mathbf{r}}_2^{RF} = (\mathbf{I} - 2\,\hat{\mathbf{n}}_{r2}^{RF}(\hat{\mathbf{n}}_{r2}^{RF})^T)\,\hat{\mathbf{r}}_1^{RF}, \tag{15}$$

where λ_{min2}^* is the minimum of the two remaining path lengths and $\hat{\mathbf{n}}_{r2}^{RF}$ is the normal of the second mirror that is hit. To find the third impact point we can just calculate the path length to the remaining surface, since it is known, or alternatively take the maximum of the path lengths to each of the three surfaces. Once this final path length is obtained the position and direction of the tertiary reflection is given by,

$$\mathbf{v}_{r3}^{RF} = \mathbf{v}_{r2}^{RF} + \lambda_{max3}^* \cdot \hat{\mathbf{r}}_2^{RF}, \tag{16}$$

$$\hat{\mathbf{r}}_3^{RF} = (\mathbf{I} - 2\,\hat{\mathbf{n}}_{r3}^{RF}(\hat{\mathbf{n}}_{r3}^{RF})^T)\,\hat{\mathbf{r}}_2^{RF}, \tag{17}$$

where λ_{max3}^* and $\hat{\mathbf{n}}_{r3}^{RF}$ are defined as before. Given that $\hat{\mathbf{n}}_{r1}^{RF}$, $\hat{\mathbf{n}}_{r2}^{RF}$, and $\hat{\mathbf{n}}_{r3}^{RF}$ are orthogonal, combining Equations (17), (15) and (13), gives,

$$\begin{aligned}\hat{\mathbf{r}}_3^{RF} &= [\mathbf{I} - 2\,\hat{\mathbf{n}}_{r1}^{RF}(\hat{\mathbf{n}}_{r1}^{RF})^T - 2\,\hat{\mathbf{n}}_{r2}^{RF}(\hat{\mathbf{n}}_{r2}^{RF})^T \\ &\qquad -2\,\hat{\mathbf{n}}_{r3}^{RF}(\hat{\mathbf{n}}_{r3}^{RF})^T]\,\hat{\mathbf{i}}_s^{RF} \\ &= [\mathbf{I} - 2\mathbf{I}]\,\hat{\mathbf{i}}_s^{RF} \\ &= -\hat{\mathbf{i}}_s^{RF}. \end{aligned} \tag{18}$$

This says that the last reflection from the corner cube is exactly parallel to the incident beam but with opposite direction. Equation (18) uses the fact that,

$$\hat{\mathbf{n}}_{r1}^{RF}(\hat{\mathbf{n}}_{r1}^{RF})^T + \hat{\mathbf{n}}_{r2}^{RF}(\hat{\mathbf{n}}_{r2}^{RF})^T + \hat{\mathbf{n}}_{r3}^{RF}(\hat{\mathbf{n}}_{r3}^{RF})^T = \mathbf{I}. \tag{19}$$

Letting $\mathbf{N} = [\hat{\mathbf{n}}_{r1}^{RF}\,\hat{\mathbf{n}}_{r2}^{RF}\,\hat{\mathbf{n}}_{r3}^{RF}]$ the left hand side of Equation (19) can be written as $\mathbf{N}\mathbf{N}^T$. Since $\mathbf{N}$ is an orthogonal matrix $\mathbf{N}^T = \mathbf{N}^{-1}$ and $\mathbf{N}\mathbf{N}^T = \mathbf{N}\mathbf{N}^{-1} = \mathbf{I}$ which proves the equality in Equation (19).

The model of the optical path used in the simulations allows for the position and orientation of the retro relative to the FSM to be changed. This allows simulation of scenarios where the clear aperture of the retro is initially outside the beam path of the pointing laser and or motion of the retro after lockup of the shear loop. Note that orientation changes of the retro only effect the determination of whether or not a return from the retro has occurred. Orientation changes of the retro do not effect the direction of the return beam as Equation (18) shows.

II.C. Shear Sensor

The design goal of the shear sensor was to make a linear sensor with enough dynamic range to detect any reflection off the face of the FSM. To achieve this a 10 mm x 10 mm position sensing detector (PSD) was used in combination with a 4.0X refractive compressor stage. The compressor was located just in front of the detector and after the dichroic beam splitter so that only the red pointing laser was visible to the detector. The compressor uses anti-reflective coatings to mitigate against ghost images.

The PSD is a two dimensional silicon detector that provides four photo currents based on the location of the center of light. Two photo currents are used to determine the center of light in one direction and the other two are used to determine the center of light in the orthogonal direction. The photo currents are proportional to both the location of the light spot and to the intensity of the light. To normalize the measurements against light intensity variations, the photo currents are amplified with a transimpedance stage and sent to an analog divider. The divider takes the sum and difference of the two photo currents associated with each direction and forms the following normalized voltage measurements,

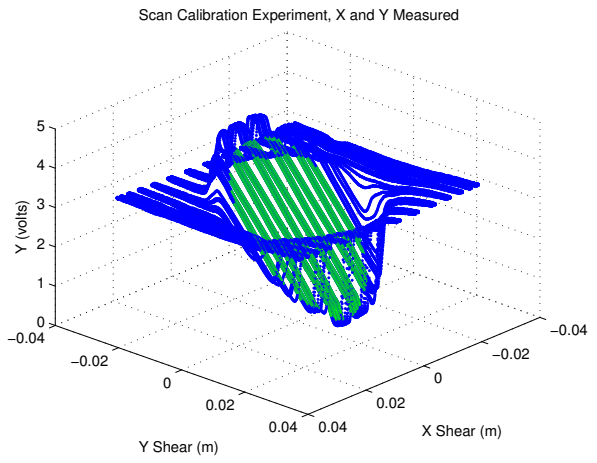

Figure 4. Acquired calibration data for the Y channel of the shear sensor. The FSM was used to scan the pointing laser (633 nm) across the full face of the retro.

$$V_{Nx} = \frac{V_{X1} - V_{X2}}{V_{X1} + V_{X2}} \tag{20}$$

$$V_{Ny} = \frac{V_{Y1} - V_{Y2}}{V_{Y1} + V_{Y2}}, \tag{21}$$

where V_{X1}, V_{X2}, V_{Y1}, and V_{Y2} are the four amplified photocurrents. The PSD essentially operates as an optical potentiometer with the two normalized voltage measurements proportional to the X and Y location

of the laser centroid. A third measurement, V_Σ, is available that gives a voltage proportional to the incident beam wattage. This measurement is used by the software to determine if a return from the retro is detected.

To calibrate this sensor, the FSM was used to scan the pointing beam across the face of the retro. The shear in this test is given by,

$$x_{Shear} \approx 4R\,\theta_{AZ} \tag{22}$$

$$y_{Shear} \approx \frac{4R}{\sqrt{2}}\theta_{EL}, \tag{23}$$

where R is the distance between the retro vertex and the center of the FSM mirror. θ_{AZ} and θ_{EL} are the gimbal angles of the FSM as measured by the Kaman sensor. Approximation symbols are used in this equation because it is a linearized model. The shear as determined by Equations (22) and (23) can be plotted versus the normalized PSD voltages. Figure 4 shows this data for V_{Ny} . Note this data is nearly linear over a diameter of 37 mm, almost the full aperture of the FSM as seen by the compressor. A plane was used to fit the data shown in the highlighted color using a least squares technique. The fitted plane is described by a point on the plane and a normal vector. With these parameters, the PSD measurements can be modeled by,

$$V_{Nx} = \hat{\mathbf{n}}_{V_{Nx}}^T(\mathbf{v}_{poxp} - \begin{bmatrix} x_{Shear} \\ y_{Shear} \\ 0 \end{bmatrix})/\,\hat{\mathbf{n}}_{V_{Nx}}(z), \tag{24}$$

$$V_{Ny} = \hat{\mathbf{n}}_{V_{Ny}}^T(\mathbf{v}_{poyp} - \begin{bmatrix} x_{Shear} \\ y_{Shear} \\ 0 \end{bmatrix})/\,\hat{\mathbf{n}}_{V_{Ny}}(z), \tag{25}$$

where $\hat{\mathbf{n}}_{V_{Nx}}$ and $\hat{\mathbf{n}}_{V_{Ny}}$ are the normal vectors and $\mathbf{v}_{poxp}$ and $\mathbf{v}_{poyp}$ are the points that reference the location of each plane. These equations are used in the simulation to model the voltages output by the sensor. For the control code we have the opposite problem to deal with. That is, given the shear voltages, V_{Nx} and V_{Ny}, determine the actual shear in physical units. This is done by simply inverting Equations (24) and (25) for x_{Shear} and y_{Shear}. Using this inversion procedure makes the gain, offset, and static coupling of the shear sensor voltages transparent to the compensator. Coupling can arise if the shear sensor measurement axes are clocked relative to the optical boresight, as defined by the direction of the FSM axes. This transparency makes design of the compensator a bit more straight forward. In addition accurate alignment of the sensor clocking becomes irrelevant.

The simulation also uses a model of the sum measurement, V_Σ. This model is zero outside the aperture of the FSM and is constant over the interior with a smooth transition between the two areas. In the code the level of this voltage is continuously monitored. If it exceeds a certain threshold, we are assured that the shear sensor measurements are valid and the shear loop can be closed to center the laser on the vertex of the retro. To build in some level of noise immunity, the sum measurements are smoothed and passed through a backlash function, prior to the threshold check.

III. Tracking Filter

The design of the compensator for the shear loop must consider both lockup transients and tracking of a moving retro.

Depending on the accuracy of the range knowledge prior to lockup, the shear servo may have to operate with poor knowledge of the loop gain. To ensure stability and minimal overshoot during lockup, the open loop transfer function must have sufficient gain margin to account for this loop gain uncertainty.

In the formation flying scenario, the disturbances during tracking are primarily caused by vehicle rotations at the base of the scanner assembly. Shear caused by motion of the retro on the target spacecraft is minimal compared to scanner motion because of the long lever arm between the two vehicles which amplifies the shear caused by small rotations of the scanner assembly. In the FCT these disturbances are ramp like in nature due to the constant velocity of the vehicle attitude between thruster firings. To null disturbances of this type with zero error, two integrators are used in the compensator. To make the open loop transfer function stable with 180 degrees of phase lag contributed by the two integrators, two phase leads are added near the open

loop crossover. In addition to adding two integrators, we also extend the bandwidth of the compensator as much as the sample rate will allow. The faster shear servo allows the loop to remain locked during changes in base body angular velocity. An open loop bandwidth of approximately 30 Hz was achieved with a shear sensor sample rate of 500 Hz. Note the actuator transfer function shown in Figure 2 has negligible phase lag up to 100 Hz and thus contributes little distortion to the open loop transfer function near the 30 Hz crossover.

We also included a ringer in the compensator at 2 Hz with a gain of 20 dB to improve tracking of sinusoidal shear commands. The gain and phase distortions of this ringer at 2 Hz do not effect the crossover region. These shear commands could be used to inject a circular dither of the pointing beam. By measuring the amount of mirror motion needed to cause the shear dither, the range can be estimated. As an example, the further the retro is from the steering mirror the less the mirror will have to move to cause a given amount of shear.

A block diagram of the pointing system is shown in Figure 5. Note the larger plant gain in the azimuth channel due to the larger sensitivity of this axis to mirror rotations. Before the shear loop is closed, the software sends an open loop spiral search command to the mirror loop. Once locked up, this command is frozen and incremental commands are sent from the shear compensator. This diagram also shows how measurements of the mirror position and shear can be used to estimate variations in the loop gain, $\hat{R}$, provided that dither commands are injected at the shear loop.

IV. Trigger Filter

The trigger filter is a simple yet effective means of using the shear sensor signal level measurement to determine whether or not a return from the retro has occurred. The output of this filter is a 1 if a detection has been made and 0 otherwise. The filter first averages the last 5 samples of the signal level, V_Σ, in the following manner,

$$V_\Sigma^f(z^{-1}) = \frac{1 + z^{-1} + z^{-2} + z^{-3} + z^{-4}}{5} V_\Sigma(z^{-1}). \tag{26}$$

This average reduces the variance of the filtered signal and provides a measure of noise immunity. After averaging the signal is then passed through a backlash operator. The output of the backlash function is initialized as 0. If the averaged signal exceeds a high threshold the output is set to 1. To be reset to zero the averaged signal must go below a low threshold. Adding the backlash operation prevents multiple transitions that would be caused by noise if a single threshold value was used for the trigger.

V. Trajectory Generation

What we desire from the search trajectory is to ensure an equal probability of detection regardless of where the retro is within the mirror field of regard. This will be accomplished if the rate at which the laser spot passes the retro is constant. To achieve this we look at how a spiral type search can be designed to achieve constant path length velocity in the search space. We first define a plane normal to the nominal line of sight of the mirror at a distance R_{nom} from the mirror as the search space. R_{nom} would be the initial guess of relative range handed off from the formation control system or alternatively one of several grid points if the knowledge is poor. In polar (r, θ) coordinates, a spiral is a curve that satisfies,

$$r = \frac{g}{2\pi}\theta \tag{27}$$

$$\theta = f(t), \tag{28}$$

where g is distance between consecutive loops of the spiral and $f(t)$ is some unspecified function of time. At any point along this curve the local velocity is given by,

$$s = \sqrt{\dot{x}^2 + \dot{y}^2}, \tag{29}$$

where $x = r\cos(\theta)$ and $y = r\sin(\theta)$. Substituting Equations (27) and (28) into Equation (29) we can arrive at the following differential equation that must be satisfied for s to be equal to some designated constant, $\bar{s}$.

$$\dot{f} = \frac{\bar{s} \cdot \frac{2\pi}{g}}{\sqrt{1 + f^2}}. \tag{30}$$

Qualitatively we should note that as f, or equivalently θ, increases, the rate of increase decreases since f appears in the denominator of Equation (30). Thus, as the radius of the spiral gets bigger the sweep rate of the angle must be reduced to keep the path length velocity constant. To generate the spiral trajectory, Equation (30) can be integrated numerically. Solving this equation forward in time will produce a counter clockwise spiral whereas a solution backward in time will produce a clockwise spiral with negative radius. By equating the x and y cartesian coordinates for the forward and backward solutions we can observe that the two trajectories have the same solution at a discrete set of common points. These points lie along the y-axis and are where the forward time solution, $\theta_{forward} = 0, \frac{\pi}{2}, \frac{3\pi}{2}, \ldots$ and the backward time solution $\theta_{backward} = 0, -\frac{\pi}{2}, -\frac{3\pi}{2}, \ldots$. These common points allow us the opportunity of transferring from an outward spiral to an inward spiral while preserving constant velocity. In this way we can loop the trajectory back on itself to keep the radius of the spiral search bounded. The transfer is accomplished by monitoring the value of $\theta_{forward}$ and resetting it at any of the above solution points to the negative of its current value. This resetting accomplishes the transfer to the backward time solution trajectory, which must then be integrated forward in time to spiral down in a continued counter clockwise fashion. The solution will evolve back down through zero and start outward again until it again reaches the desired reset value. The reset value of $\theta_{forward}$ needs to be chosen so that the stroke of the FSM is not exceeded.

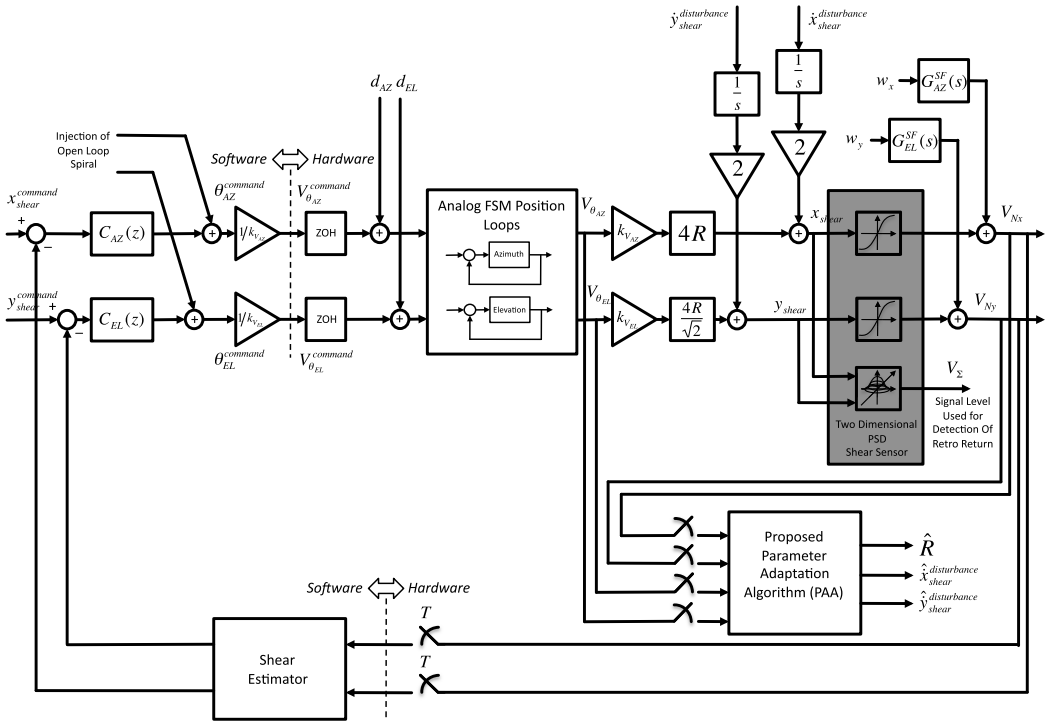

Figure 5. Diagram of optical pointing sensor servo loops showing local analog servos of the fast steering mirror and outer shear sensor loop. During open loop search for the retro, the shear loop is broken and the spiral search trajectory is injected from within the software directly to the FSM commands. The signal level voltage is used to determine if the shear loop can be closed. The shear estimator, shown in the feedback path, uses a plane fit of sensor calibration data to invert the gain, offset, and coupling of the sensor voltages.

To implement the above trajectory we must transform our knowledge of the curve in the search space to mirror commands. To go from x-y coordinates in our search space to mirror angles we can use the following

approximations,

$$\theta_{AZ} \approx \frac{1}{2R_{nom}}\, x \tag{31}$$

$$\theta_{EL} \approx \frac{\sqrt{2}}{2R_{nom}}\, y. \tag{32}$$

As a rule of thumb, the spacing parameter g in Equation (27) should be chosen to be less then or equal to the dynamic range of the shear sensor, which in the search space, is roughly 20 millimeters. The parameter $\bar{s}$ in Equation (30) is limited by the sample rate of the sensor. It must be small enough to ensure a fine grid spacing of sampled points on the search spiral.

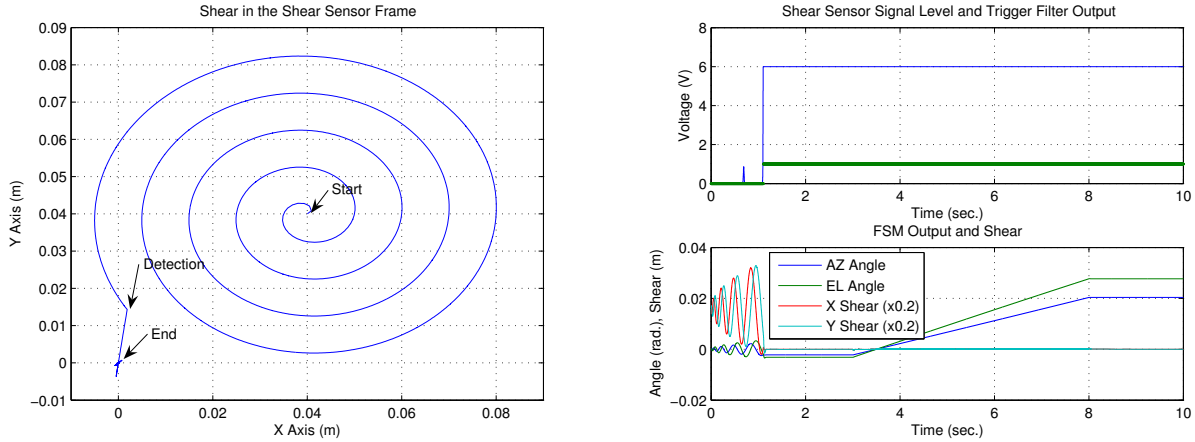

(a) (b)

Figure 6. (a) Shear at the shear sensor during search, detection, and lockup of the shear sensor. (b) Top: Shear sensor signal level and trigger filter output during open loop search and tracking of the retro. Bottom: FSM steering angles and shear servo error during open loop search and tracking of a moving retro.

VI. Simulations

In order to prototype the control software a virtual simulation environment was constructed. This environment included models of the FSM dynamics, models of the three shear sensor outputs V_{Nx}, V_{Ny}, and V_{Σ}, and optical models of the reflection at the FSM and corner cube. The control software interfaced to these models using 16 bit A/D measurements of the shear sensor voltages and 16 bit D/A mirror angle commands. The simulation executed the control software at 500 Hz.

In this virtual environment, the vertex of the retro was placed 4.5 meters away from the FSM along the nominal boresight and offset by 0.0283 meters in a direction perpendicular to the nominal boresight. In this configuration, the pointing laser initially misses the retro. The software responds by initiating a spiral search until the trigger filter detects a return from the retro. Once detection of the retro is made the shear loop is closed with a command of zero, drawing the pointing laser to the vertex of the retro. After the servo error is nulled the retro is then moved, at t = 3.0 seconds, with a constant velocity of 0.062 meters per second, in a plane perpendicular to the nominal boresight. The motion is stopped at t = 8.0 seconds, 0.283 meters from the nominal boresight. The simulation ends at t = 10.0 seconds. This test sequence is shown in Figure 6a. This Figure plots the shear that would be present at the compressor assuming no limitations on the size of the retro and FSM mirror. This Figure shows the image of the spiral search and lockup of the tracking filter as the search nears the offset location of the retro vertex.

The top portion of Figure 6b shows the shear sensor signal level and trigger filter output during the same test sequence. Note the near miss just prior to the lockup. At the near miss the return beam hits on the edge of the FSM mirror. Only a portion of the beam is reflected to the shear sensor causing a weak signal level. The spiral search continued on the outward trajectory for another full revolution before lockup occurred. The shear servo error and FSM commands are shown in the bottom of Figure 6b. Note the servo error is nulled just after lockup and is kept small even during movement of the retro. Note also the change in the

FSM servo commands during motion and subsequent tracking of the retro position.

In this simulation the controller was given perfect knowledge of the distance between the retro and FSM. The lateral motion in this test case contributed very little to deviations in this distance. Although this test case did not address uncertainty in this distance, we can expect the shear servo to remain stable for relatively large uncertainties since the Bode plots have significant gain margin. Large changes in this distance during operation without using corrections from the rangefinder make the plant time varying and any notion of stability using Bode analysis is no longer appropriate.

VII. Experimental Results

Benchtop laboratory tests of the pointing system are shown in Figure 7. As in the simulation, the trigger and tracking filters are implemented at 500 Hz with a TI TMS320C6713 floating point DSP. Sampling of the shear sensor and commanding of the mirror angles are done with 16 bits of resolution. To mimic the simulation scenario, the retro was placed just outside the nominal boresight of the FSM so that no return from the retro is observed. With no signal level on the shear sensor the software initiates the open loop scan using the trajectories generated by Equations (31) and (32). These commands are converted to voltage levels and sent out the DAC to the FSM servo electronics. These are the azimuth and elevation servo commands shown in Figure 7.

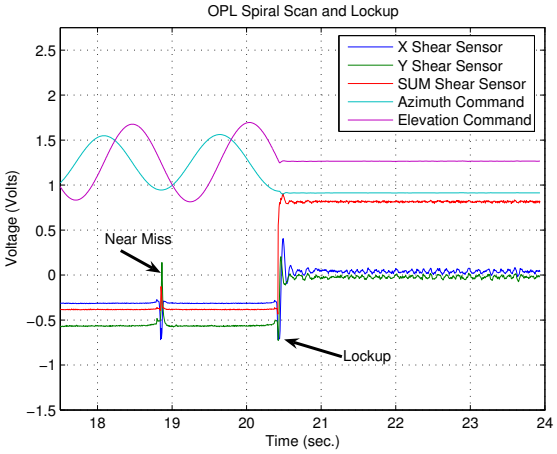

Figure 7. Spiral scan and lockup of the optical pointing loop (OPL). The test sequence shows the spiral scan commands and shear sensor signals before lockup and after a return from the far field retro has been detected and the pointing loop closed.

The software continues the open loop scan until the signal level, V_Σ, at the shear sensor exceeds the preset threshold used by the trigger filter. As in the simulation, note the near miss in Figure 7 where the retro is hit, but the shear induced is partially beyond the aperture of the FSM. The spiral trajectory continues after this near miss until the return is fully within the aperture of the FSM. The high signal level at the shear sensor causes the trigger filter to change its state from a 0 to 1. When this happens the software pauses the spiral search and closes the shear servo with a command input of zero. This servo nulls the shear so that the pointing laser is drawn from the perimeter of the retro to its center. This lockup event is indicated in Figure 7 at t = 20.4 seconds. Note the shear signals being drive to zero and the high value of the signal level at this event. Note also that after the shear servo is closed, the azimuth and elevation commands to the FSM are the last value of the spiral trajectory plus whatever incremental values are calculated by the shear servo.

The data in Figure 7 demonstrates search and lockup of a fixed retro. After lockup if the retro where then moved within the field of regard (FOR) of the FSM, the shear servo would act to track the center of the retro by keeping the servo error small. If the motion of the retro where to exceed the bandwidth of the shear servo then lock on the center could not be guaranteed.

VIII. Conclusions and Future Works

In this paper we have demonstrated a fully functional sensor system capable of giving vector measurements to a remote retro target. This system was developed with formation flying in mind, but may have other applications such as rendezvous and docking and terrain mapping. The rangefinder has been integrated into the optical path and does give valid range measurements, but integration of the serial port of this device with the DSP is not completed at this time. In addition, calibration of the bearing measurements would have to be done prior to integration with the FCT robots. This could be done by tracking a retro with the scanner system and with a Leica laser tracker simultaneously. The laser tracker is capable of giving extremely accurate position measurements which can be associated with the FSM sensor measurements to establish a lookup table for the bearing in a frame attached to the scanner. Depending on the amount of

effort used to model the bearing as a function of the FSM measurements, a conservative estimate of the accuracy of the bearing information would be 1 part per 1000 of the 12 degree field of regard (full cone) of the FSM or 43.2 arc seconds. The accuracy of the range information is limited by the performance of the SICK laser rangefinder. According to the manufacturer documentation it is accurate to ± 1.0 centimeter within 10 meters. Statistical error is 1.0 millimeter (1-sigma).

Injecting a circular dither command to the shear loop is another way to estimate range. The accuracy of this estimate would depend on independent calibration of both the FSM sensor and shear sensor. Moreover, since the necessary FSM motion to inject a given amount of shear is inversely proportional to the range the FSM sensor calibration error will map to a larger and larger error in the range as the absolute value of the range increases. These two problems make dithering an unlikely method of accurate range determination. Dithering to get range is, however, good enough for the purposes of control where uncertainty on the order of 1 part 10 is acceptable. Using either range estimates or measurements from the rangefinder in the shear loop compensation is an interesting control problem that deserves further study and research. Several known methods of adaptive control could potentially be applied to this problem to make the performance of the shear loop invariant to changes in the distance to the retro.

As a final remark we note that the search trajectory designed in section V is circular but that the field of regard of the FSM in the search space is elliptical. This limits the diameter of the circular search to the minor axis of this ellipse. Clearly a search that is elliptical and has constant path length velocity would be desired over the existing trajectory.

IX. Acknowledgments

The work described in this paper was carried out at the Jet Propulsion Laboratory, California Institute of Technology, under contract with the National Aeronautics and Space Administration.

References

[1]Ljung, L., *System Identification Theory For the User*, Prentice Hall Information and System Sciences Series, 1987.

[2]Murray, R., Li, Z., and Sastry, S., *A Mathematical Introduction to Robotic Manipulation*, CRC Press, 1994.

[3]Shields, J., "External Delay and Delay Rate Estimation for the Formation Interferometer Testbed (FIT)," Engineering memorandum em-3457-03-001, Jet Propulsion Laboratory, Feb. 2003.